MOX–Report No. 34/2010

A mimetic finite difference method for Large Eddy Simulation of incompressible flow

Antonella Abba', Luca Bonaventura

MOX, Dipartimento di Matematica "F. Brioschi"
Politecnico di Milano, Via Bonardi 9 - 20133 Milano (Italy)

mox@mate.polimi.it http://mox.polimi.it

A mimetic finite difference method for Large Eddy Simulation of incompressible flow

Antonella Abbà [♯] , Luca Bonaventura [♯]

August 18, 2010

[♯] MOX – Modellistica e Calcolo Scientifico
Dipartimento di Matematica "F. Brioschi"
Politecnico di Milano
via Bonardi 9, 20133 Milano, Italy
antonella.abba@polimi.it, luca.bonaventura@polimi.it

Keywords: Navier-Stokes equations, incompressible flow, turbulence simulations, mimetic discretizations, computational fluid dynamics

AMS Subject Classification: 35Q30, 65M06, 76M20, 76B47, 76D05, 76D10

Abstract

A finite difference discretization of the three-dimensional, incompressible Navier-Stokes equations is presented, based on finite difference operators that satisfy discrete analogs of some basic calculus identities. These mimetic properties yield a numerical method for which a discrete form of the vorticity equation can be derived naturally from the discrete momentum equation, by application of the mimetic rotation operator. As a result, a discrete approximation of vorticity is exactly preserved, for inviscid flows, independently of the mesh size. The vorticity preservation property guarantees that no spurious vorticity is generated by the nonlinear advective terms in absence of viscosity. A mimetic discretization of the viscous terms and an appropriate treatment for rigid wall boundary conditions are also proposed. The relationship of this approach to other similar techniques is discussed. The proposed method is validated on several idealized test cases for laminar incompressible flow, in which it is compared to a widely used finite difference discretization. The method is then applied to Large Eddy Simulation of incompressible flow, demonstrating the advantages of the inherent conservation properties in a comparison with experimental data and DNS results especially when strong vorticity production takes place at the boundaries.

1 Introduction

The development of numerical methods for fluid flow preserving discrete analogs of some invariants of the equations of motion (such as e.g. mass, momentum, energy, enstrophy) attracted great attention in the early phases of computational fluid dynamics. In particular, finite differencing techniques possessing such properties were developed in context of numerical models for large scale atmospheric flows, see e.g. [5], [6], [20], [27], [36], [37]. Also more recent work has devoted attention to these discrete properties, see e.g. [8], [9], [10], [18], [26], [28], [29], [33], [35], [39], [40]. The development of numerical methods with discrete conservation properties can take advantage of the so called *mimetic* finite difference schemes, for which discrete analogs of continuous identies hold, such as $\nabla \times \nabla \phi = 0$, integration by parts formulae and the Helmholtz decomposition theorem. Examples of mimetic finite differences are given e.g. by [19], [31], in two and three dimensional frameworks, respectively. These properties have been used e.g. in [32] to prove stability and convergence of the MAC discretization approach.

Some evidence of the benefits of these conservative approaches is given by the consistent reproduction of energy and enstrophy spectra in long term decaying turbulence simulations, as proposed e.g. in [10], [11], [35]. In more conventional CFD applications, the arguments supporting the use of mimetic schemes are also related to the desire of reproducing correct turbulence spectra, the discussion in [33]. Furthermore, it was suggested in [29] that apparently pathological solutions of the Euler equations may indeed be the result of spurious vorticity production, which could be avoided if vorticity preserving discretizations were employed.

In this paper, we will investigate numerically a vorticity preserving discretization for incompressible flow problems, with the aim of assessing its potential advantages with respect to more common discretization approaches for large eddy simulation (LES) applications. In particular, a MAC-type, mass and vorticity preserving finite difference discretization of the three dimensional Navier-Stokes equations will be used, based on the concepts first proposed in [36] for the shallow water equations and extended more recently in [10] to triangular meshes. Vorticity preservation means that a discrete vorticity equation can be achieved by application of a mimetic *curl* operator to the discrete momentum equation. As a consequence, the spatial semi-discretization preserves discrete irrotational initial data in absence of viscosity. Furthermore, both the viscous term and the rigid wall boundary conditions are discretized consistently in a vorticity preserving manner. These particular features of the discretization are achieved at the same computational cost of more standard approaches and ensure that no spurious vorticity is produced by the numerical solution procedure. The resulting numerical method is very similar to other techniques based on analogous mimetic concepts. For example, a three-dimensional extension of the original Sadourny's approach was first introduced in [37] for models of nonhydrostatic atmospheric flows.

The purpose of this paper is not so much to introduce an entirely novel discretization approach, as to highlight the advantages of the vorticity preserving numerical techniques with respect to other methods of the same order of accuracy that either do not preserve any discrete invariant or have other discrete preservation properties. A number of numerical experiments will show that the proposed discretization concept produces remarkable improvements with respect to a more conventional numerical method that is of the same order and only differs from our mimetic scheme for the discretization of the nonlinear momentum advection term. The accuracy improvement appears to be especially significant in regimes where highly localized vorticity production is taking place close to boundaries. Furthermore, results of a high Reynolds number LES computation are presented and compared to corresponding experimental data and Direct Numerical Simulation results, showing a remarkable improvement in accuracy as a consequence of the inherent conservation properties of the proposed method. These findings seem to warrant the conjecture formulated in [29] that vorticity preservation may indeed be beneficial. Preliminary results obtained with the present discretization in laminar flow tests were presented in [1], [2].

In section 2, several formulations of the incompressible Navier-Stokes equation are briefly reviewed and a specific dynamic subgrid scale model is introduced, that will be employed in the LES computations. The basic operators of the proposed finite difference discretization are introduced in section 3, while the vorticity preserving spatial discretization and its properties are described in section 4. The discretization of the boundary conditions is discussed in section 5. In section 6, the results of various tests for inviscid or laminar flows are shown, demonstrating the substantial advantages of the proposed technique with respect to another widely used finite difference method of comparable accuracy. In sections 7 and 8, the application of the method to LES is presented, for which also distinctive advantages are displayed with respect to traditional techniques. Some conclusions from the comparisons carried out so far and on the perspectives for future developments are presented in section 9.

2 The Navier-Stokes equations

The Navier-Stokes equations for a constant density, incompressible fluid can be written as

$$\frac{\partial \mathbf{u}}{\partial t} = -\mathbf{u} \cdot \nabla \mathbf{u} - \nabla p + \mu \Delta \mathbf{u} \tag{1}$$

$$\nabla \cdot \mathbf{u} = 0 \tag{2}$$

for $\mathbf{x} \in \Omega$, where Ω is a bounded region in $\mathbf{R}^3$, $\mathbf{u}$ denotes the flow velocity and p the pressure field. For the purpose of deriving vorticity preserving discretizations, a reformulation of these equations is considered, based on the identities (see e.g.[12])

$$\mathbf{u} \cdot \nabla \mathbf{u} = \boldsymbol{\omega} \times \mathbf{u} + \nabla K, \tag{3}$$

$$\Delta \mathbf{u} = \nabla(\nabla \cdot \mathbf{u}) - \nabla \times \boldsymbol{\omega}, \tag{4}$$

where $\boldsymbol{\omega} = \nabla \times \mathbf{u}$ denotes vorticity and $K = \|\mathbf{u}\|^2/2$ denotes kinetic energy. The Navier-Stokes equations can be rewritten as

$$\frac{\partial \mathbf{u}}{\partial t} = -\boldsymbol{\omega} \times \mathbf{u} - \nabla(p + K) - \mu \nabla \times \boldsymbol{\omega} \tag{5}$$

$$\nabla \cdot \mathbf{u} = 0 \tag{6}$$

Taking the curl of the momentum equation, an evolution equation for vorticity can also be obtained

$$\frac{\partial \boldsymbol{\omega}}{\partial t} = -\nabla \times \Big[\boldsymbol{\omega} \times \mathbf{u}\Big] + \mu \Delta \boldsymbol{\omega}. \tag{7}$$

For applications to Large Eddy Simulation (LES) of turbulent flows, the filtered Navier-Stokes equations will be considered

$$\frac{\partial \tilde{\mathbf{u}}}{\partial t} = -\tilde{\boldsymbol{\omega}} \times \tilde{\mathbf{u}} - \nabla(\tilde{p} + \tilde{K}) - \mu \nabla \times \tilde{\boldsymbol{\omega}} - \nabla \cdot \tau_{SGS} \tag{8}$$

$$\nabla \cdot \tilde{\mathbf{u}} = 0 \tag{9}$$

where the tilde denotes the implicit filtering operation over the grid and τ_{SGS} is the subgrid scale (SGS) stress tensor. Dynamic models for τ_{SGS} have been first proposed in [15], to which we refer for the complete definition of the notation

and of the corresponding basic concepts. Here, the mixed anisotropic tensor model proposed and validated in [3] will be used, that can be described as an extension of the isotropic dynamic model (see e.g. [25]).

The mixed anisotropic SGS tensor is defined by

$$\tau_{ij} - (\delta_{ij}/3)\sum_k \tau_{kk} = L_{ij} \quad - \quad (\delta_{ij}/3)\sum_k L_{kk} \tag{10}$$
$$- \quad 2\sum_{r,s} B_{ijrs}\tilde{\Delta}^2|\tilde{S}|\tilde{S}_{rs} + \frac{2}{3}\delta_{ij}\sum_{k,r,s} B_{kkrs}\tilde{\Delta}^2|\tilde{S}|\tilde{S}_{rs}$$

where L_{ij} is the resolved turbulent stress tensor. The fourth order tensor B_{ijrs} is assumed to have the following form:

$$B_{ijrs} = \sum_{\alpha,\beta} C_{\alpha\beta} a_{i\alpha} a_{j\beta} a_{r\alpha} a_{s\beta} \tag{11}$$

and $a_{i\alpha}$ are the components of unit vectors $\mathbf{a}_\alpha(\alpha$ =1,2,3), to be chosen suitably. The 3×3 matrix $a_{i\alpha}$ is unitary; in particular $a^{-1} = a^T$, where a^T is the transposed matrix. $C_{\alpha\beta} = C_{\beta\alpha}$ are the elements of a 3×3 symmetric matrix. Note that the usual sum convention has not been used for obvious reasons. The coefficients $C_{\alpha\beta}$ vary in space and time. The assumption is that, in the locally rotated reference frame defined by the transformation matrices $a_{i\alpha}$, the tensor B_{ijrs} becomes diagonal with respect to 2 indices. Using the Germano identity, the coefficients $C_{\alpha\beta}$ are determined explicitly in function of the resolved velocity field. In this paper, the eigenvectors of the L tensor have been used as unit vectors a_i of the local reference frame.

3 Finite difference discrete operators

A staggered discretization grid with at most $N_x \times N_y \times N_z$ computational cells is introduced, along the lines of popular discretization methods such as the MAC (marker and cell) approach, introduced in [17], or the Arakawa C grid (see e.g. [5]). Each cell is numbered at its center with indices i, j and k, for the x, y and z directions, respectively. The length of the cell sides in each directions are denoted by Δx_i, Δy_j and Δz_k and they are assumed to vary in their respective direction only. The cell volume is given by $V_{i,j,k} = \Delta x_i \Delta y_j \Delta z_k$ and staggered spacings $\Delta x_{i+\frac{1}{2}}$ are defined by arithmetic average.

The discrete u velocity is defined at half integer i and integers j and k, v is defined at integers i, k and half integer j, while w is defined at integers i, j and half integers k. Finally, p and all other three-dimensional scalar variables are defined at integers i, j, k. At points where they are not defined, the discrete variables are generally computed by simple arithmetical mean of the nearest defined values. Averaged quantities will usually be denoted by an overbar, so that e.g.

$$\bar{u}_{i,j,k} = \frac{u_{i+\frac{1}{2},j,k} + u_{i-\frac{1}{2},j,k}}{2},$$

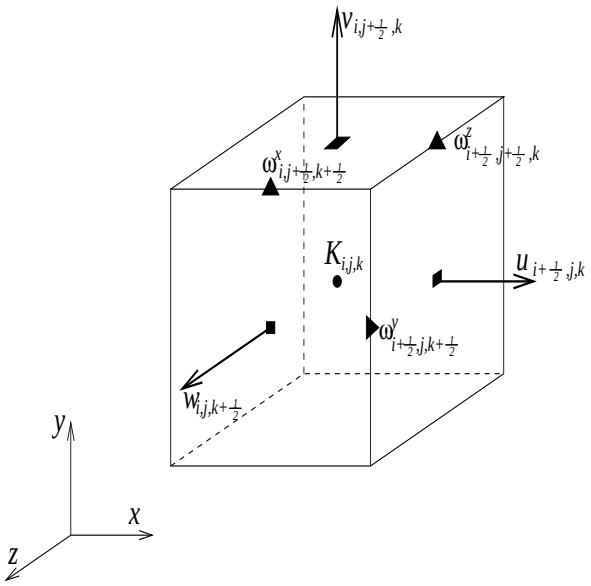

Figure 1: Location of velocity and vorticity point on the staggered Cartesian mesh.

$$\bar{u}_{i,j+\frac{1}{2},k} = \frac{u_{i+\frac{1}{2},j,k} + u_{i-\frac{1}{2},j,k} + u_{i+\frac{1}{2},j+1,k} + u_{i-\frac{1}{2},j+1,k}}{4}.$$

Difference operators are then introduced as

$$\delta_x \phi_{i+\frac{1}{2},j,k} = \frac{\phi_{i+1,j,k} - \phi_{i,j,k}}{\Delta x_{i+\frac{1}{2}}} \qquad \delta_x \phi_{i,j,k} = \frac{\phi_{i+\frac{1}{2},j,k} - \phi_{i-\frac{1}{2},j,k}}{\Delta x_i}$$

$$\delta_y \phi_{i,j+\frac{1}{2},k} = \frac{\phi_{i,j+1,k} - \phi_{i,j,k}}{\Delta y_{j+\frac{1}{2}}} \qquad \delta_y \phi_{i,j,k} = \frac{\phi_{i,j+\frac{1}{2},k} - \phi_{i,j-\frac{1}{2},k}}{\Delta y_j}$$

$$\delta_z \phi_{i,j,k+\frac{1}{2}} = \frac{\phi_{i,j,k+1} - \phi_{i,j,k}}{\Delta z_{k+\frac{1}{2}}} \qquad \delta_z \phi_{i,j,k} = \frac{\phi_{i,j,k+\frac{1}{2}} - \phi_{i,j,k-\frac{1}{2}}}{\Delta z_k}$$

for staggered and unstaggered locations, respectively.
A discrete divergence operator is also defined at unstaggered locations as

$$\begin{aligned} \mathrm{div}(u,v,w)_{i,j,k} \quad &= \frac{u_{i+\frac{1}{2},j,k} - u_{i-\frac{1}{2},j,k}}{\Delta x_i} \\ &+ \frac{v_{i,j+\frac{1}{2},k} - v_{i,j-\frac{1}{2},k}}{\Delta y_j} + \frac{w_{i,j,k+\frac{1}{2}} - w_{i,j,k-\frac{1}{2}}}{\Delta z_k}. \end{aligned} \tag{12}$$

With a similar definition, the divergence operator can be also defined at any staggered location, if the components of a discrete vector field normal to the

faces of the corresponding control volume are available. The vorticity fluxes are naturally defined via the Stokes theorem at the faces of staggered control volumes, so that

$$\begin{aligned}
\omega^x_{i,j+\frac{1}{2},k+\frac{1}{2}} &= \frac{w_{i,j+1,k+\frac{1}{2}} - w_{i,j,k+\frac{1}{2}}}{\Delta y_{j+\frac{1}{2}}} - \frac{v_{i,j+\frac{1}{2},k+1} - v_{i,j+\frac{1}{2},k}}{\Delta z_{k+\frac{1}{2}}} \\
\omega^y_{i+\frac{1}{2},j,k+\frac{1}{2}} &= \frac{u_{i+\frac{1}{2},j,k+1} - u_{i+\frac{1}{2},j,k}}{\Delta z_{k+\frac{1}{2}}} - \frac{w_{i+1,j,k+\frac{1}{2}} - w_{i,j,k+\frac{1}{2}}}{\Delta x_{i+\frac{1}{2}}} \\
\omega^z_{i+\frac{1}{2},j+\frac{1}{2},k} &= \frac{v_{i+1,j+\frac{1}{2},k} - v_{i,j+\frac{1}{2},k}}{\Delta x_{i+\frac{1}{2}}} - \frac{u_{i+\frac{1}{2},j+1,k} - u_{i+\frac{1}{2},j,k}}{\Delta y_{j+\frac{1}{2}}}.
\end{aligned} \tag{13}$$

A discrete *curl* operator can be defined for each cell as

$$\mathrm{curl}(u,v,w)_{i,j,k} = (\omega^x_{i,j+\frac{1}{2},k+\frac{1}{2}}, \omega^y_{i+\frac{1}{2},j,k+\frac{1}{2}}, \omega^z_{i+\frac{1}{2},j+\frac{1}{2},k}). \tag{14}$$

These definitions are similar to those given e.g. in [19] and have similar mimetic properties. More specifically, we first prove that

$$\mathrm{curl}(\delta_x\phi, \delta_y\phi, \delta_z\phi)_{i,j,k} = 0. \tag{15}$$

Indeed, applying equations (13) to the discrete vector field components given by $\delta_x\phi_{i+\frac{1}{2},j,k}$, $\delta_y\phi_{i,j+\frac{1}{2},k}$, $\delta_z\phi_{i,j,k+\frac{1}{2}}$ one obtains e.g. for the vorticity flux in the x direction

$$\begin{aligned}
\omega^x_{i,j+\frac{1}{2},k+\frac{1}{2}} &= \frac{\delta_z\phi_{i,j+1,k+\frac{1}{2}} - \delta_z\phi_{i,j,k+\frac{1}{2}}}{\Delta y_{j+\frac{1}{2}}} - \frac{\delta_y\phi_{i,j+\frac{1}{2},k+1} - \delta_y\phi_{i,j+\frac{1}{2},k}}{\Delta z_{k+\frac{1}{2}}} \\
&= \frac{1}{\Delta y_{j+\frac{1}{2}}\Delta z_{k+\frac{1}{2}}}[\phi_{i,j+1,k+1} - \phi_{i,j+1,k} - \phi_{i,j,k+1} + \phi_{i,j,k} \\
&-\phi_{i,j+1,k+1} + \phi_{i,j,k+1} + \phi_{i,j+1,k} - \phi_{i,j,k}] = 0.
\end{aligned}$$

Analogous calculations for the other vorticity components yield equation (15). The second key mimetic property is

$$\mathrm{div}(\omega^x, \omega^y, \omega^z)_{i+\frac{1}{2},j+\frac{1}{2},k+\frac{1}{2}} = 0. \tag{16}$$

This can be proven showing that the expression on the left hand side of equation (16) can be expanded as

$$\begin{aligned}
&\frac{\omega^x_{i+1,j+\frac{1}{2},k+\frac{1}{2}} - \omega^x_{i,j+\frac{1}{2},k+\frac{1}{2}}}{\Delta x_{i+\frac{1}{2}}} \quad + \frac{\omega^y_{i+\frac{1}{2},j+1,k+\frac{1}{2}} - \omega^y_{i+\frac{1}{2},j,k+\frac{1}{2}}}{\Delta y_{j+\frac{1}{2}}} \\
&\qquad\qquad + \frac{\omega^z_{i+\frac{1}{2},j+\frac{1}{2},k+1} - \omega^z_{i+\frac{1}{2},j+\frac{1}{2},k}}{\Delta z_{k+\frac{1}{2}}},
\end{aligned}$$

which in turn can be rewritten as

$$\begin{aligned}
&\frac{w_{i+1,j+1,k+\frac{1}{2}} - w_{i+1,j,k+\frac{1}{2}}}{\Delta y_{j+\frac{1}{2}} \Delta x_{i+\frac{1}{2}}} - \frac{v_{i+1,j+\frac{1}{2},k+1} - v_{i+1,j+\frac{1}{2},k}}{\Delta z_{k+\frac{1}{2}} \Delta x_{i+\frac{1}{2}}} \\
&- \frac{w_{i,j+1,k+\frac{1}{2}} - w_{i,j,k+\frac{1}{2}}}{\Delta y_{j+\frac{1}{2}} \Delta x_{i+\frac{1}{2}}} + \frac{v_{i,j+\frac{1}{2},k+1} - v_{i,j+\frac{1}{2},k}}{\Delta z_{k+\frac{1}{2}} \Delta x_{i+\frac{1}{2}}} \\
&+ \frac{u_{i+\frac{1}{2},j+1,k+1} - u_{i+\frac{1}{2},j+1,k}}{\Delta z_{k+\frac{1}{2}} \Delta y_{j+\frac{1}{2}}} - \frac{w_{i+1,j+1,k+\frac{1}{2}} - w_{i,j+1,k+\frac{1}{2}}}{\Delta x_{i+\frac{1}{2}} \Delta y_{j+\frac{1}{2}}} \\
&- \frac{u_{i+\frac{1}{2},j,k+1} - u_{i+\frac{1}{2},j,k}}{\Delta z_{k+\frac{1}{2}} \Delta y_{j+\frac{1}{2}}} + \frac{w_{i+1,j,k+\frac{1}{2}} - w_{i,j,k+\frac{1}{2}}}{\Delta x_{i+\frac{1}{2}} \Delta y_{j+\frac{1}{2}}} \\
&+ \frac{v_{i+1,j+\frac{1}{2},k+1} - v_{i,j+\frac{1}{2},k+1}}{\Delta x_{i+\frac{1}{2}} \Delta z_{k+\frac{1}{2}}} - \frac{u_{i+\frac{1}{2},j+1,k+1} - u_{i-\frac{1}{2},j,k+1}}{\Delta y_{j+\frac{1}{2}} \Delta z_{k+\frac{1}{2}}} \\
&- \frac{v_{i+1,j+\frac{1}{2},k} - v_{i,j+\frac{1}{2},k}}{\Delta x_{i+\frac{1}{2}} \Delta z_{k+\frac{1}{2}}} + \frac{u_{i+\frac{1}{2},j+1,k} - u_{i-\frac{1}{2},j,k}}{\Delta y_{j+\frac{1}{2}} \Delta z_{k+\frac{1}{2}}} = 0.
\end{aligned}$$

Equation (16) can also be rewritten as e.g.

$$\delta_x \omega^x_{i+\frac{1}{2},j+\frac{1}{2},k+\frac{1}{2}} = -\delta_y \omega^y_{i+\frac{1}{2},j+\frac{1}{2},k+\frac{1}{2}} - \delta_z \omega^z_{i+\frac{1}{2},j+\frac{1}{2},k+\frac{1}{2}}. \tag{17}$$

It is to be remarked that the above definitions and properties hold for staggered locations belonging to the interior of an arbitrarily shaped computational domain. For nodes at the boundaries, the definition of the vorticity value depends on the boundary conditions being imposed. The discrete boundary conditions for the present formulation are described in section 5. However, the definition given at the boundary is consistent with the definition of operator 14, since it is derived along the same lines as discrete analog of of Stokes theorem.

4 A mimetic spatial discretization of the Navier-Stokes equations

The proposed spatial discretization of equations (5)-(6) is obtained by application of the mimetic finite difference operators described in the previous section:

$$\frac{\partial}{\partial t}u_{i+\frac{1}{2},j,k} = -\bar{\omega}^{y}_{i+\frac{1}{2},j,k}\bar{w}_{i+\frac{1}{2},j,k} + \bar{\omega}^{z}_{i+\frac{1}{2},j,k}\bar{v}_{i+\frac{1}{2},j,k} - \delta_x(p+\bar{K})_{i+\frac{1}{2},j,k} + \mu\Big[\delta_z(\omega^y)_{i+\frac{1}{2},j,k} - \delta_y(\omega^z)_{i+\frac{1}{2},j,k}\Big] \tag{18}$$

$$\frac{\partial}{\partial t}v_{i,j+\frac{1}{2},k} = -\bar{\omega}^{z}_{i,j+\frac{1}{2},k}\bar{u}_{i,j+\frac{1}{2},k} + \bar{\omega}^{x}_{i,j+\frac{1}{2},k}\bar{w}_{i,j+\frac{1}{2},k} - \delta_y(p+\bar{K})_{i,j+\frac{1}{2},k} + \mu\Big[\delta_x(\omega^z)_{i,j+\frac{1}{2},k} - \delta_z(\omega^x)_{i,j+\frac{1}{2},k}\Big] \tag{19}$$

$$\frac{\partial}{\partial t}w_{i,j,k+\frac{1}{2}} = -\bar{\omega}^{x}_{i,j,k+\frac{1}{2}}\bar{v}_{i,j,k+\frac{1}{2}} + \bar{\omega}^{y}_{i,j,k+\frac{1}{2}}\bar{u}_{i,j,k+\frac{1}{2}} - \delta_z(p+\bar{K})_{i,j,k+\frac{1}{2}} + \mu\Big[\delta_y(\omega^x)_{i,j,k+\frac{1}{2}} - \delta_x(\omega^y)_{i,j,k+\frac{1}{2}}\Big] \tag{20}$$

$$\mathrm{div}(u,v,w)_{i,j,k} = 0. \tag{21}$$

The resulting method, that is second order accurate in space in the case of constant mesh spacing, extends to the three-dimensional, viscous, incompressible case the techniques proposed in [9], [10] for the discretization of the shallow water equations on a triangular geodesic grid. These were in turn inspired by the seminal paper [36] and by the methods presented in [26]. A similar three-dimensional extension was first introduced in [37] for models of nonhydrostatic atmospheric flows. In the two-dimensional inviscid case, the discretization (18)-(21) coincides exactly with that of [36], if constant fluid thickness is assumed in the shallow water equations considered therein. On the other hand, the choice of the formulation (5)-(6) leads to a formulation that is similar to that of [33]. The main difference between the present approach and the discretization proposed in [33] lies in the location of the velocity and vorticity points. In the present discretization, the tangential velocity components at the cell edge (for example, the terms $\bar{w}_{i+\frac{1}{2},j,k}, \bar{v}_{i+\frac{1}{2},j,k}$ in equation 18) are averaged separately at the edge midpoint, while in [33] the whole momentum advection term is computed at the cell vertex (i.e., at the discrete location where vorticity is defined).

The proposed discretization is mass and vorticity preserving. Indeed, mass conservation is achieved in the same way as in the standard MAC approach. In order to prove vorticity preservation we will show that, taking the discrete *curl* of equations (18)-(20), a consistent discretization of equation (7) results. More specifically, one has e.g.

$$
\begin{aligned}
&\frac{\partial}{\partial t}\omega^x_{i,j+\frac{1}{2},k+\frac{1}{2}} \\
&= \frac{1}{\Delta y_{j+\frac{1}{2}}}\Big\{ - \bar{\omega}^x_{i,j+1,k+\frac{1}{2}}\bar{v}_{i,j+1,k+\frac{1}{2}} + \bar{\omega}^y_{i,j+1,k+\frac{1}{2}}\bar{u}_{i,j+1,k+\frac{1}{2}} \\
&-\delta_z(p+\bar{K})_{i,j+1,k+\frac{1}{2}} + \mu\Big[\delta_y(\omega^x)_{i,j+1,k+\frac{1}{2}} - \delta_x(\omega^y)_{i,j+1,k+\frac{1}{2}}\Big] \\
&+\bar{\omega}^x_{i,j,k+\frac{1}{2}}\bar{v}_{i,j,k+\frac{1}{2}} - \bar{\omega}^y_{i,j,k+\frac{1}{2}}\bar{u}_{i,j,k+\frac{1}{2}} \\
&+\delta_z(p+\bar{K})_{i,j,k+\frac{1}{2}} - \mu\Big[\delta_y(\omega^x)_{i,j,k+\frac{1}{2}} - \delta_x(\omega^y)_{i,j,k+\frac{1}{2}}\Big]\Big\} \\
&-\frac{1}{\Delta z_{k+\frac{1}{2}}}\Big\{ - \bar{\omega}^z_{i,j+\frac{1}{2},k+1}\bar{u}_{i,j+\frac{1}{2},k+1} + \bar{\omega}^x_{i,j+\frac{1}{2},k+1}\bar{w}_{i,j+\frac{1}{2},k+1} \\
&-\delta_y(p+\bar{K})_{i,j+\frac{1}{2},k+1} + \mu\Big[\delta_x(\omega^z)_{i,j+\frac{1}{2},k+1} - \delta_z(\omega^x)_{i,j+\frac{1}{2},k+1}\Big] \\
&+\bar{\omega}^z_{i,j+\frac{1}{2},k}\bar{u}_{i,j+\frac{1}{2},k} - \bar{\omega}^x_{i,j+\frac{1}{2},k}\bar{w}_{i,j+\frac{1}{2},k} \\
&+\delta_y(p+\bar{K})_{i,j+\frac{1}{2},k} - \mu\Big[\delta_x(\omega^z)_{i,j+\frac{1}{2},k} - \delta_z(\omega^x)_{i,j+\frac{1}{2},k}\Big]\Big\}
\end{aligned}
$$

Consider now that the pressure gradient terms cancel because of equation (15) and that one can rewrite the diffusive terms as

$$
\begin{aligned}
&\frac{1}{\Delta y_{j+\frac{1}{2}}}\Big\{\mu\Big[\delta_y(\omega^x)_{i,j+1,k+\frac{1}{2}} - \delta_x(\omega^y)_{i,j+1,k+\frac{1}{2}}\Big] \\
&-\mu\Big[\delta_y(\omega^x)_{i,j,k+\frac{1}{2}} - \delta_x(\omega^y)_{i,j,k+\frac{1}{2}}\Big]\Big\} \\
&-\frac{1}{\Delta z_{k+\frac{1}{2}}}\Big\{\mu\Big[\delta_x(\omega^z)_{i,j+\frac{1}{2},k+1} - \delta_z(\omega^x)_{i,j+\frac{1}{2},k+1}\Big] \\
&-\mu\Big[\delta_x(\omega^z)_{i,j+\frac{1}{2},k} - \delta_z(\omega^x)_{i,j+\frac{1}{2},k}\Big]\Big\} \\
&= \frac{\mu}{\Delta y_{j+\frac{1}{2}}}\Big\{\delta_y(\omega^x)_{i,j+1,k+\frac{1}{2}} - \delta_y(\omega^x)_{i,j,k+\frac{1}{2}}\Big\} \\
&+\frac{\mu}{\Delta z_{k+\frac{1}{2}}}\Big\{\delta_z(\omega^x)_{i,j+\frac{1}{2},k+1} - \delta_z(\omega^x)_{i,j+\frac{1}{2},k}\Big\} \\
&+\frac{\mu}{\Delta y_{j+\frac{1}{2}}}\Big\{ - \delta_x(\omega^y)_{i,j+1,k+\frac{1}{2}} + \delta_x(\omega^y)_{i,j,k+\frac{1}{2}}\Big\} \\
&-\frac{\mu}{\Delta z_{k+\frac{1}{2}}}\Big\{\delta_x(\omega^z)_{i,j+\frac{1}{2},k+1} - \delta_x(\omega^z)_{i,j+\frac{1}{2},k}\Big\}.
\end{aligned}
$$

Exploiting the fact that

$$\begin{aligned}
&\frac{\mu}{\Delta y_{j+\frac{1}{2}}}\Big\{ -\delta_x(\omega^y)_{i,j+1,k+\frac{1}{2}} + \delta_x(\omega^y)_{i,j,k+\frac{1}{2}} \Big\} \\
&-\frac{\mu}{\Delta z_{k+\frac{1}{2}}}\Big\{ \delta_x(\omega^z)_{i,j+\frac{1}{2},k+1} - \delta_x(\omega^z)_{i,j+\frac{1}{2},k} \Big\} \\
&= \frac{\mu}{\Delta x_i}\Big\{ -\delta_y\omega^y_{i+\frac{1}{2},j+1,k+\frac{1}{2}} + \delta_y\omega^y_{i-\frac{1}{2},j+1,k+\frac{1}{2}} \\
&-\delta_z\omega^z_{i+\frac{1}{2},j+1,k+\frac{1}{2}} + \delta_z\omega^z_{i-\frac{1}{2},j+1,k+\frac{1}{2}} \Big\},
\end{aligned}$$

using (17) and repeating the corresponding steps also for equations (19)-(20) one obtains finally

$$\begin{aligned}
\frac{\partial}{\partial t}\omega^x_{i,j+\frac{1}{2},k+\frac{1}{2}} \quad &= -\delta_y[\bar{\omega}^x\bar{v} - \bar{\omega}^y\bar{u}]_{i,j+\frac{1}{2},k+\frac{1}{2}} + \delta_z[\bar{\omega}^z\bar{u} - \bar{\omega}^x\bar{w}]_{i,j+\frac{1}{2},k+\frac{1}{2}} \\
&+\mu\ \mathrm{div}(\delta_x\omega^x, \delta_y\omega^x, \delta_z\omega^x)_{i,j+\frac{1}{2},k+\frac{1}{2}} \qquad (22) \\
\frac{\partial}{\partial t}\omega^y_{i+\frac{1}{2},j,k+\frac{1}{2}} \quad &= -\delta_z[\bar{\omega}^y\bar{w} - \bar{\omega}^z\bar{v}]_{i+\frac{1}{2},j,k+\frac{1}{2}} + \delta_x[\bar{\omega}^x\bar{v} - \bar{\omega}^y\bar{u}]_{i+\frac{1}{2},j,k+\frac{1}{2}} \\
&+\mu\ \mathrm{div}(\delta_x\omega^y, \delta_y\omega^y, \delta_z\omega^y)_{i+\frac{1}{2},j,k+\frac{1}{2}} \qquad (23) \\
\frac{\partial}{\partial t}\omega^z_{i+\frac{1}{2},j+\frac{1}{2},k} \quad &= -\delta_x[\bar{\omega}^z\bar{u} - \bar{\omega}^x\bar{w}]_{i+\frac{1}{2},j+\frac{1}{2},k} + \delta_y[\bar{\omega}^y\bar{w} - \bar{\omega}^z\bar{v}]_{i+\frac{1}{2},j+\frac{1}{2},k} \\
&+\mu\ \mathrm{div}(\delta_x\omega^z, \delta_y\omega^z, \delta_z\omega^z)_{i+\frac{1}{2},j+\frac{1}{2},k} \qquad (24)
\end{aligned}$$

Equations (22)-(24) represent a consistent spatial discretization of equation (7). It should be noticed that similar results are true also for more conventional schemes. For example, in the two dimensional case, discretizing momentum advection by upwind finite differences and applying the curl operator, by lengthy but straightforward algebra one obtains a numerical scheme for the vorticity advection equation that is equivalent to an upwind discretization of the two dimensional analog of (7) plus a first order source term. The same derivation is carried out in Appendix 1 of [38] for a MAC scheme using centered finite differences for the discretization of momentum advection. In that case, a second order source term results. The key difference between vorticity preserving approaches as the one analyzed here and other discretizations lies in the fact that no such mesh and flow dependent source terms are present for the vorticity preserving schemes. As a result, in absence of boundaries and assuming an initial state such that $\mathrm{curl}(u, v, w)_{i,j,k} = 0$, equations (22)-(24) imply that the discrete vorticity remains zero also at any later time. Thus, no spurious vorticity is produced by the spatial discretization, independently of the mesh size. It can be observed that in the two dimensional case, the present scheme reduces to the (potential) enstrophy preserving scheme of [36], so that the same enstrophy conservation proof holds assuming the fluid thickness to be constant in the shallow water equations considered by [36]. The numerical tests presented in section 6

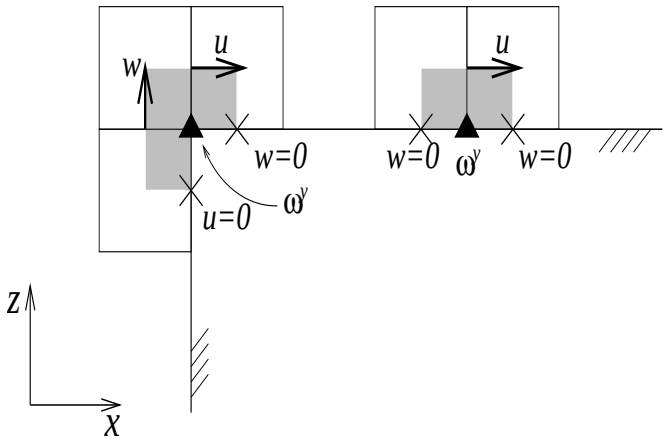

Figure 2: Computation of vorticity values at the boundaries.

will show that this vorticity preserving scheme has in practice good enstrophy preservation properties.

5 Discretization of rigid wall boundary condition

At the boundaries of the computational domain, boundary conditions have to be imposed and a discretization procedure must be found that is appropriate to provide discrete boundary values for equations (18)-(21). We consider here rigid wall, no slip conditions, which are usually applied to the Navier-Stokes equations (see e.g. [12]). The rigid wall condition is imposed by assuming that the normal velocity components at the boundary faces are zero. In the discretization approach described by equations (18)-(21), the only other boundary conditions that need to be assigned are the values of the vorticity fluxes $\omega^x_{i,j+\frac{1}{2},k+\frac{1}{2}}, \omega^y_{i+\frac{1}{2},j,k+\frac{1}{2}}, \omega^z_{i+\frac{1}{2},j+\frac{1}{2},k}$ for cell edges that belong to boundary faces. These boundary vorticity values are computed by applying Stokes theorem (see fig. 2) to control volumes adjacent to the boundary and whose boundary faces are centered at the discrete locations where vorticity fluxes are defined. In particular, along the boundary faces the tangential velocity component is assumed to be zero, in agreement with the no slip boundary condition.

6 Validation on idealized cases of laminar flow

A full space-time discretization can be obtained from the spatial discretization introduced in section 4, by application of an appropriate time stepping scheme. For the purpose of the tests discussed in this paper, a third order Runge-Kutta method was employed for time discretization of the advective terms, along with a second order Runge-Kutta method for the diffusive terms (see the dis-

cussion in [38] on the stability of Runge-Kutta schemes for the discretization of advection equation). As a result, a scheme of overall second order accuracy in time is obtained. To enforce the incompressibility constraint, a projection method was employed (see e.g. [4], [16], [22], [34]), with an explicit predictor step using the above described time discretization and a following pressure correction step, in which a Poisson equation is solved for pressure to ensure that the discrete velocity field is divergence free. For all the numerical tests considered, relatively small values of the timestep and of the Courant number were used, since the focus here is on the investigation of the properties of the spatial discretization.

Throughout this section, the results of the vorticity preserving scheme are compared to those obtained in the same test cases with another finite difference method for the discretization of the nonlinear momentum equation. More specifically, the centered finite difference method of [24] has been employed, coupled to the same time discretization described above. The spatial discretization of [24] is also second order in space, mass conservative and uses the same MAC type staggered grid and the same discretization of the divergence operator. It only differs from our approach in the approximation of the momentum equation, which does not preserve vorticity in the sense described in section 4. The implementation of the finite difference method of [24] used for these tests had been validated previously in a number of laminar and turbulent flow simulations (see e.g. [3]). In the following paragraphs, the reference finite difference method of [24] will be denoted as scheme 1, while the vorticity preserving method of section 4 will be denoted as scheme 2.

6.1 Lamb dipole

In the first numerical experiment, the two-dimensional Lamb dipole is studied numerically. The Lamb dipole consists of two symmetric patterns with vorticity of opposite sign. Using polar coordinates r, θ, inside the circular region with radius $r = a$ vorticity is given by

$$\omega = -\frac{2U_0}{J_0(ka)} J_1(kr) \sin\theta, \tag{25}$$

where J_n is the $n-$th order Bessel function of the first kind and k is chosen so that $ka \approx 3.8317$ is the first zero of J_1. Outside the circle $r \leq a$, the motion is irrotational with uniform velocity $\mathbf{u} = (U_0, 0, 0)$. In the inviscid case, the dipole moves along the axis with a constant velocity U_0 and without changing shape. Moreover, vorticity, kinetic energy and enstrophy are conserved. This problem has been solved on a domain of size $L_x = L_z = 6$ with 256×256 grid points. Periodic boundary conditions in x and free slip conditions in z have been applied. The values $U_0 = 2$ and $a = 1$ are chosen for the initial vorticity field. We observe that kinetic energy (graph not shown) is well conserved by both numerical schemes. On the other hand, scheme 1 does display spurious

production of vorticity (see fig.3,4) and enstrophy (see fig.5.), while scheme 2 does indeed preserve well the vorticity minima, maxima and mean values.

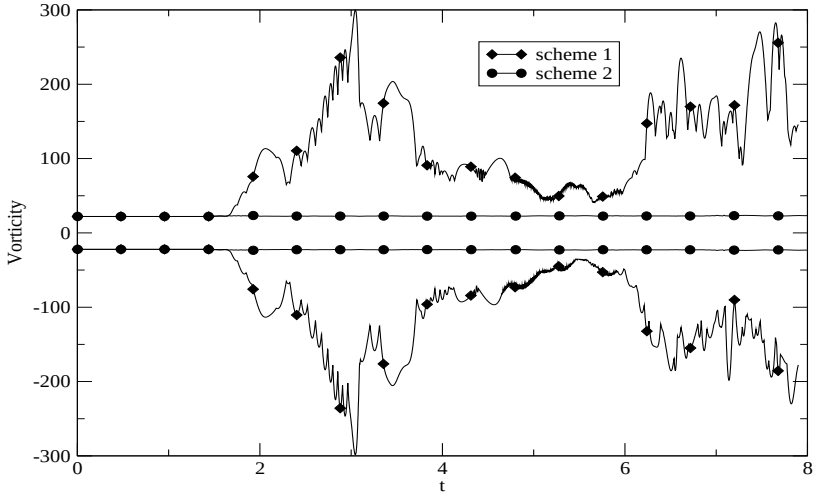

Figure 3: Time evolution of minimum and maximum vorticity for the inviscid Lamb dipole.

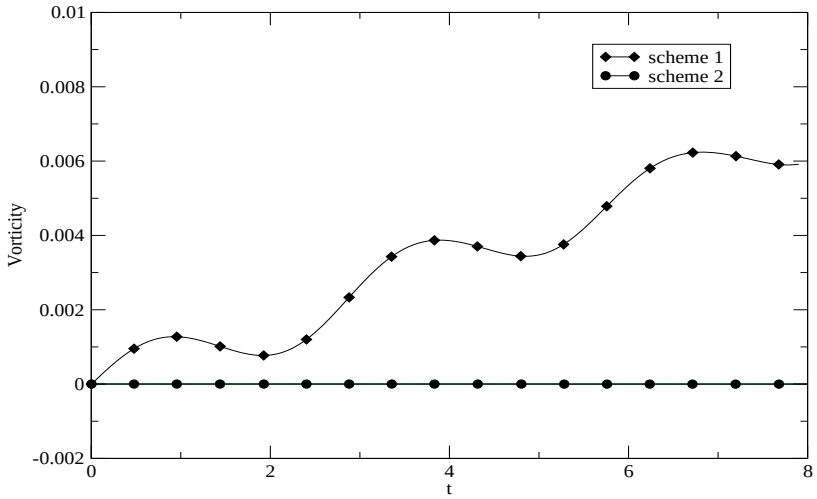

Figure 4: Time evolution of mean vorticity for the inviscid Lamb dipole.

The vorticity plots in figures 6,7 also show that a great amount of spurious vorticity is produced close to the symmetry axis by scheme 1, while scheme 2 appears to conserve much better the vorticity structure of the dipole.

As a consequence, the velocity field obtained with the scheme 1 is much noisier than that of the scheme 2, see figures 8, 9.

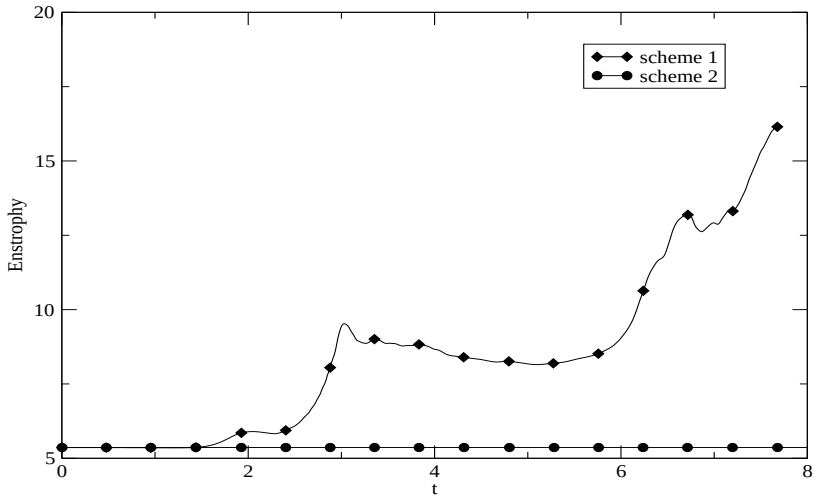

Figure 5: Time evolution of mean enstrophy for the inviscid Lamb dipole.

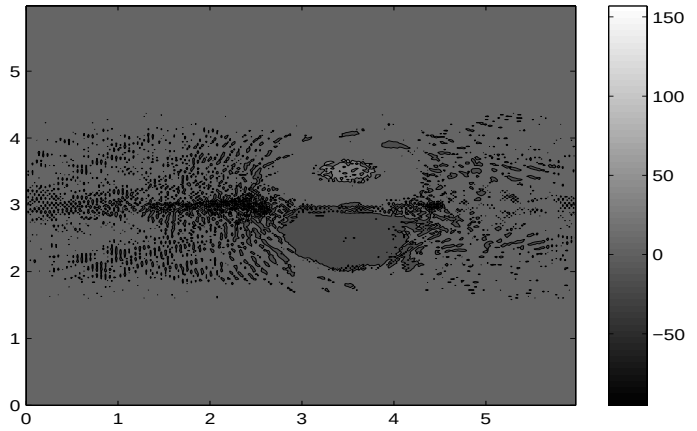

Figure 6: Vorticity field obtained with standard finite difference scheme for the inviscid Lamb dipole.

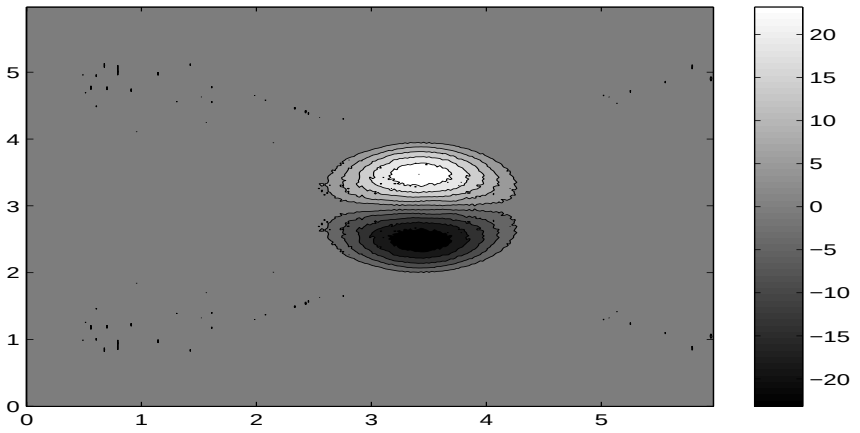

Figure 7: Vorticity field obtained with vorticity preserving mimetic scheme for the inviscid Lamb dipole.

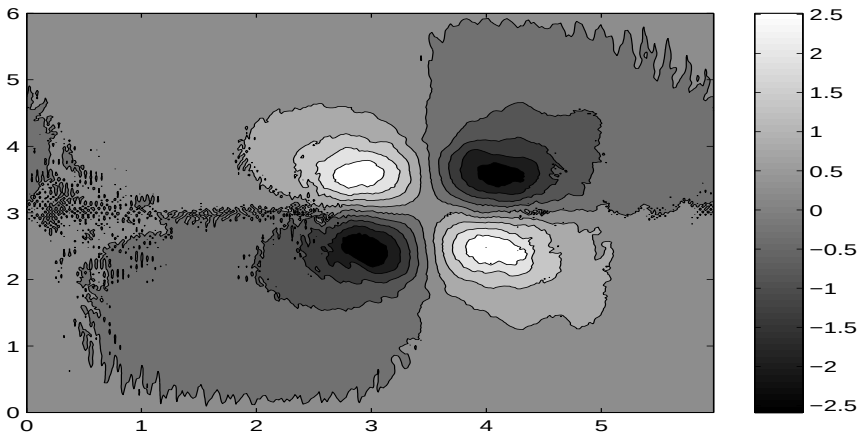

Figure 8: Vertical velocity field obtained with standard finite difference scheme for the inviscid Lamb dipole.

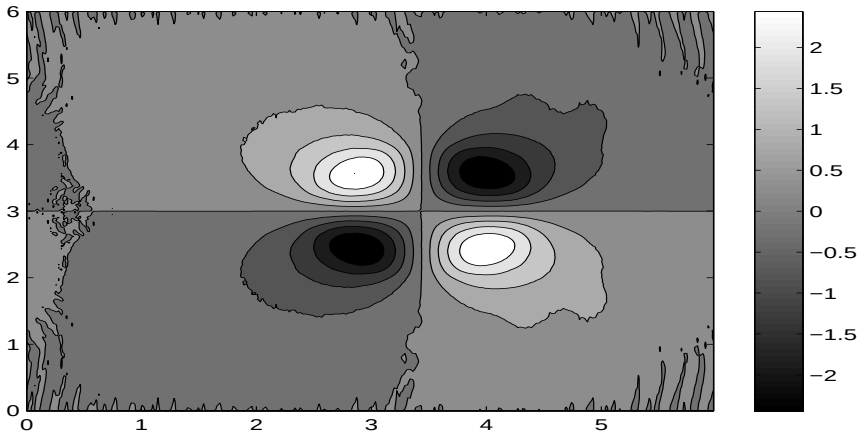

Figure 9: Vertical velocity field obtained with vorticiy preserving mimetic scheme for the inviscid Lamb dipole.

6.2 ABC flow

The Arnold - Beltrami - Childress (ABC) flow (see e.g. [7], [14]) was then considered, which provides a nonlinear test for the Navier-Stokes equations in which an analytic solution is known, at least in the inviscid case. The velocity field of the ABC flow is given by

$$\begin{aligned} u &= A\sin z + C\cos y \\ v &= B\sin x + A\cos z \\ w &= C\sin y + B\cos x. \end{aligned} \tag{26}$$

It is a three dimensional, periodic velocity field associated to a vorticity satisfying the relation $\boldsymbol{\omega} = \mathbf{u}$. Field (26) is an analytic solution of the Euler equations. Thus, we can use the numerical simulation of the ABC flow to evaluate the accuracy of the spatial discretization scheme for the convective term in a strongly three dimensional field. Periodic boundary conditions are applied in all space directions, so that the results are not affected by the approximation of the boundary conditions. The computational domain is a cubic box of 2π size with $50 \times 50 \times 50$ grid cells. The flow constants were taken to be $A = B = C = 1$. For such a flow, the mean kinetic energy and the mean enstrophy are given by

$$\bar{K} = \frac{1}{8\pi^3}\int_0^{2\pi}\int_0^{2\pi}\int_0^{2\pi}\frac{1}{2}\left(u^2+v^2+w^2\right)dxdydz = \frac{3}{2}$$

$$\bar{\eta} = \frac{1}{8\pi^3}\int_0^{2\pi}\int_0^{2\pi}\int_0^{2\pi}\frac{1}{2}\left(\omega_x^2+\omega_y^2+\omega_z^2\right)dxdydz = \frac{3}{2},$$

respectively. ABC flows may very rapidly become unstable, but, if no disturbances or dissipation are introduced, the predicted values for mean kinetic energy and enstrophy should be conserved during the simulation. Thus, any deviation of the computed values from the predicted ones is a measure of the error of the numerical scheme. In figures 10, 11, the results for the inviscid Euler case are shown. The graph for the kinetic energy in figure 10 shows that scheme 1 is indeed dissipative, while the solution obtained with scheme 2 shows an increasing kinetic energy. The enstrophy is initially dumped by scheme 1, (fig.11), with a rapid increment at a later time. On the other hand, scheme 2 appears to stay much closer to the correct value on the same time range.

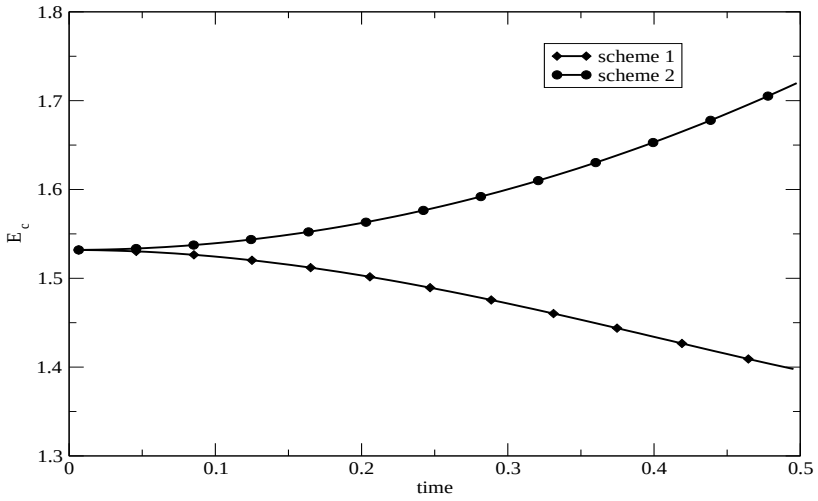

Figure 10: Time evolution of mean kinetic energy for the solution of inviscid ABC flow.

If an external driving force $\mathbf{f} = \mathbf{u}/Re$ is imposed, field (26) is again a solution of the Navier-Stokes equations. Otherwise (see e.g. [14]), the flow decays as $e^{(-\frac{t}{Re})}\mathbf{u}$. At very low Reynolds number ($Re < 13.044$) the solution is stable. In order to test the accuracy of the diffusive term approximation, the simulation of the ABC flow has been performed also in the viscous case.

In figures 12,13, the mean kinetic energy and enstrophy obtained with the two schemes, are compared to the theoretical values in the case in which no external forcing was applied. As in the inviscid case, the two methods have opposite behaviour concerning energy dissipation, while the vorticity preserving scheme is clearly more accurate in reproducing the total enstrophy decay.

7 Large eddy simulation of plane channel turbulent flow

The correct representation of wall turbulence and the accurate prediction of

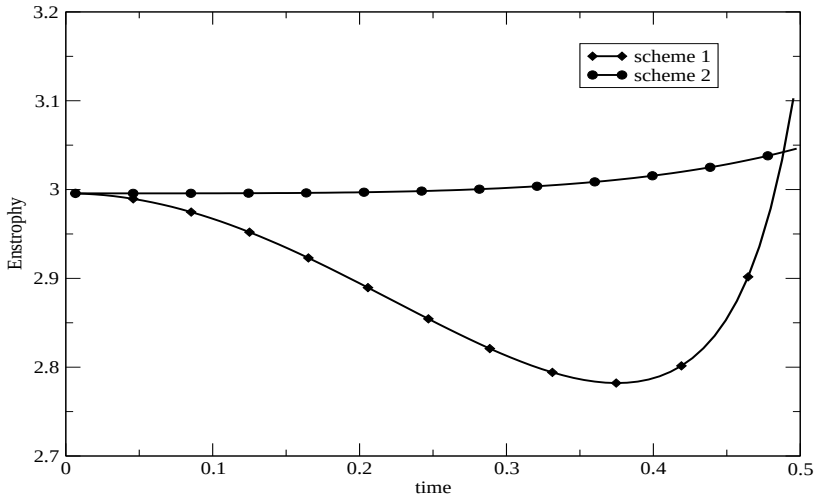

Figure 11: Time evolution of mean enstrophy for the solution of inviscid ABC flow.

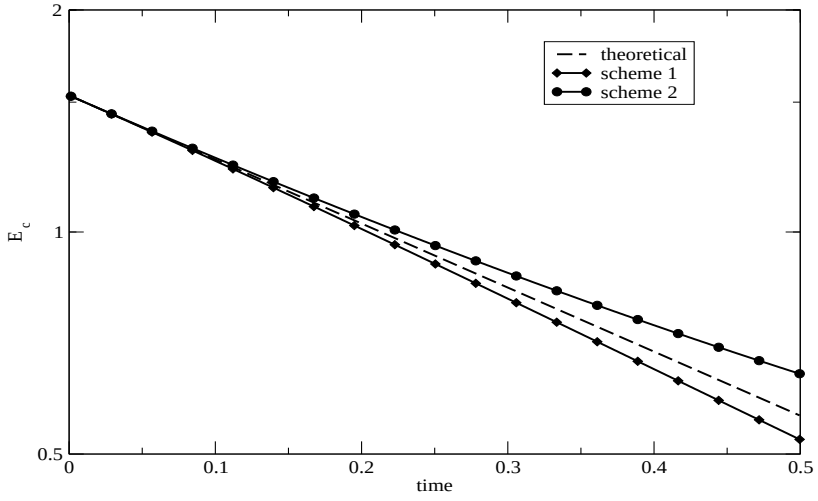

Figure 12: Time evolution of mean kinetic energy for the solution of viscous ABC flow without driving force at Reynolds number $Re = 1$.

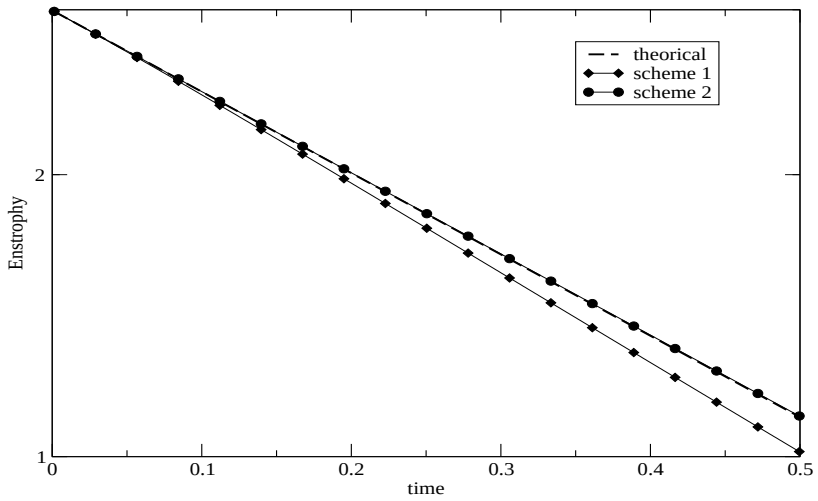

Figure 13: Time evolution of mean enstrophy for the solution of viscous ABC flow without driving force at Reynolds number $Re = 1$.

skin friction are of great importance for various engineering and environmental applications. For this reason, in order to assess the potential advantages of the proposed method for numerical simulation of turbulent flows, the classical plane channel flow has been considered as a benchmark. For such a flow, Large Eddy Simulation employing the anisotropic mixed model (10) has been performed. We consider plane-channel flow at Reynolds number $Re_\tau = \frac{u_\tau \delta}{\nu} = 180$, based on the half height of the channel δ, and on the friction velocity $u_\tau = \sqrt{\tau_w/\rho}$, where τ_w is the mean shear stress at the wall. The channel flow is simulated in a computational box with dimensionless size $L_x = 2\pi$ in the streamwise direction x and $L_y = \pi$ in the spanwise direction. No-slip walls are located at $z = \pm 1$. The flow is forced in streamwise direction with a volume forcing such that the mass flow is constant during the simulation. Periodic boundary conditions are used in streamwise and spanwise directions. The corresponding Reynolds $Re = \frac{U_{max}\delta}{\nu}$ number based on the maximum streamwise velocity has an expected value of $Re = 3290$. The resolution used is $N_x = N_y = 32$ and $N_z = 27$. In the normal direction, the grid is stretched using a tanh function; there are three points in the laminar sublayer, and eight points within the buffer region. In the horizontal direction the grid spacing in wall units is 17.7×8.8. The simulations are started from a divergence - free random perturbations field superimposed to a logaritmic velocity profile. After a sufficiently long transient, a statistically steady state is reached, after which statistical averaging is performed over about 40 nondimensional time units.

The results obtained with the mimetic scheme (denoted as scheme 2) are compared to the results obtained with a DNS [30] and to the experimental data in [42], [23], and to the results obtained by a simulation performed using our

numerical code with the scheme 1. For the two schemes, we evaluated the skin friction error defined as

$$\delta_\tau = \frac{\tau_w/U_b^2 - \tau_{ref}/U_{b_{ref}}^2}{\tau_{ref}/U_{b_{ref}}^2},$$

where the DNS results have been used as a reference (U_b is the bulk velocity). The δ_τ errors are not so different for the two schemes, yielding $\delta_\tau = 0.2289$ for scheme 1 and $\delta_\tau = 0.2225$ for scheme 2.

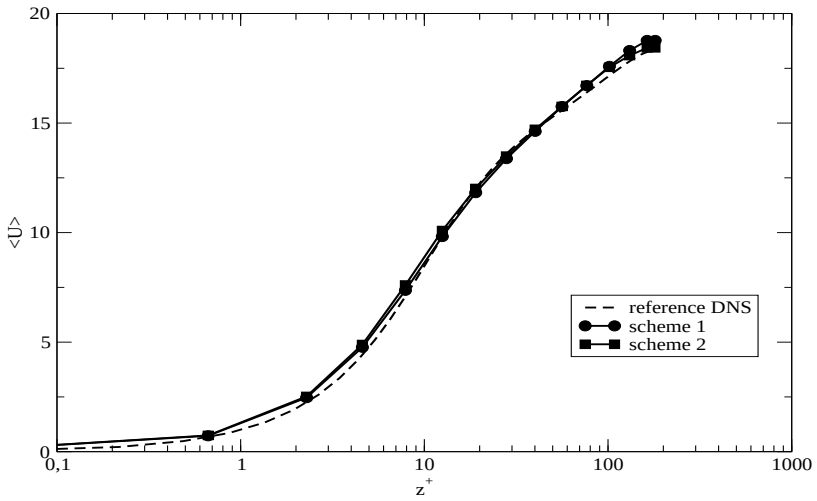

Figure 14: Mean streamwise velocity profile for channel flow at $Re_\tau = 180$.

In fig.14 we show the longitudinal mean velocity profile as a function of the distance from the walls expressed in wall units,z^+, where $z^+ = \frac{zu_\tau}{\nu}$; the results for both scheme 1 and scheme 2 are in good agreement with velocity profile obtained by the DNS. Also the profiles for the root mean square of velocity fluctuation (figg.15,16,17) are similar for the two schemes, and both are in better agreement with experimental data than DNS results. As a conclusion, results of the plane channel test show a an essentially equivalent performance of schemes 1 and 2.

8 Large eddy simulation of three-dimensional turbulent flow over an obstacle

In order to assess the potential advantages of the proposed method for numerical simulation of turbulent flows when strong vorticity production takes place at the boundaries, the flow in a channel with a square cylinder on the lower wall has been considered as a benchmark. All the variables are nondimensionalized by the bulk velocity above the cylinder and the height H of the obstacle. The computational domain is a box of size $L_x = 16$, $L_y = 2\pi$, $L_z = 2$ with $150 \times 34 \times 82$

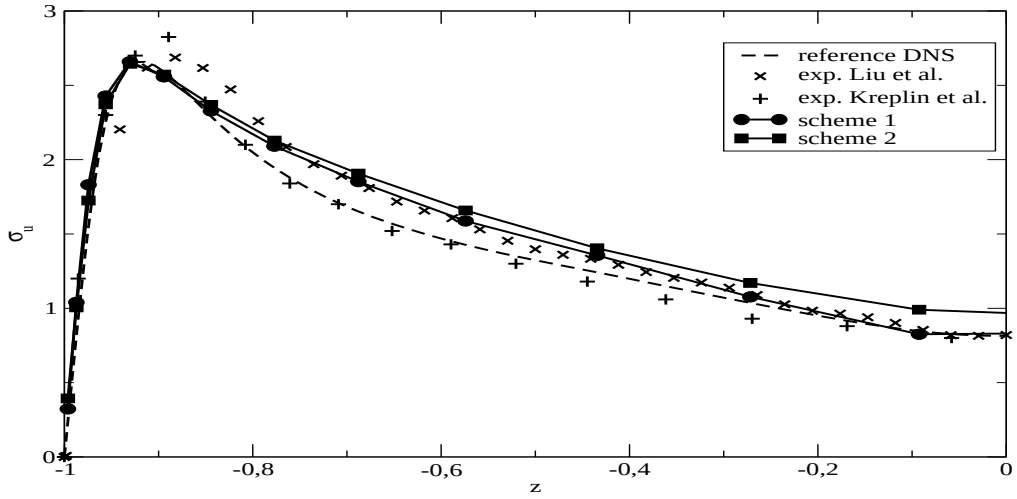

Figure 15: Root mean square of the streamwise velocity fluctuation profile for channel flow at $Re_\tau = 180$.

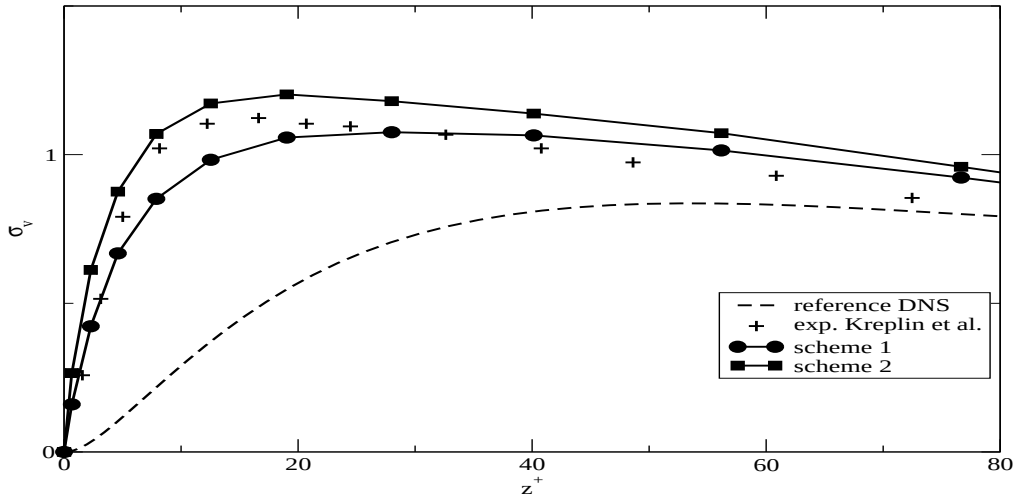

Figure 16: Root mean square of the spanwise velocity fluctuation profile for channel flow at $Re_\tau = 180$.

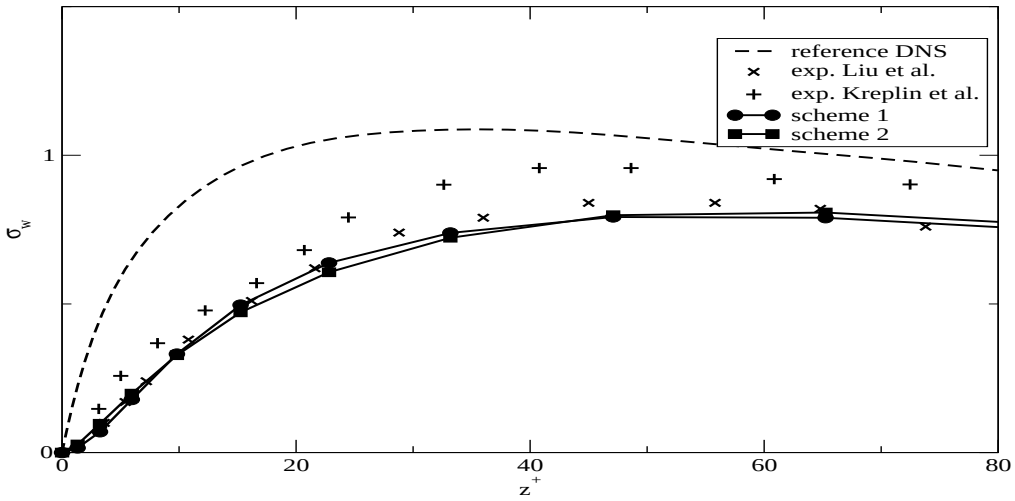

Figure 17: Root mean square of the normal to the wall velocity fluctuation profile for channel flow at $Re_\tau = 180$.

mesh points, respectively. The square cylinder is placed at $5 \leq x \leq 6$. The minimum grid size close to the obstacle is $\Delta x_{min} = 0.009$ $\Delta z_{min} = 0.002$, while grid size increases away from the cylinder. Periodic boundary conditions are assumed in the x and y directions, while no slip conditions for the velocity and Neumann condition for the pressure are imposed at the walls.

The flow has been simulated at Reynolds numbers $Re = 3000$ and $Re = 5000$. In fig.18, a schematic rendering of the separation and reattachment regions around the cylinder is shown, as defined by the zero contours of the average streamwise velocity. There are primary and secondary separation and reattachment regions, both upstream and downstream of the obstacle. Moreover, a tertiary separation zone is present at the downstream corner between the obstacle and the wall. For the given Reynolds numbers, reattachment does not occur at the top of the obstacle.

Firstly, the results for $Re = 3000$ are shown. Table 8 gives the values of the separation and reattachment lengths indicated in figure 18, as computed with scheme 1, scheme 2 and in the LES and DNS results of [41]. It can be noticed that the values for the separation and reattachment lengths are, in most cases, better evaluated by scheme 2. Fig.18 can be qualitatively compared with the two instantaneous velocity fields obtained with scheme 1 and scheme 2 (fig.19): also in the instantaneous velocity field is visible that the scheme 1 underestimates the separation and reattachment lengths.

From fig.20 can be observed that the scheme 1 does not reproduce the tertiary separation zone in the downstream corner.

Fig.21 shows a noise production in the streamwise vorticity component on the upstream corner for the scheme 1.

Averaged longitudinal and vertical velocity profiles, at different x coordi-

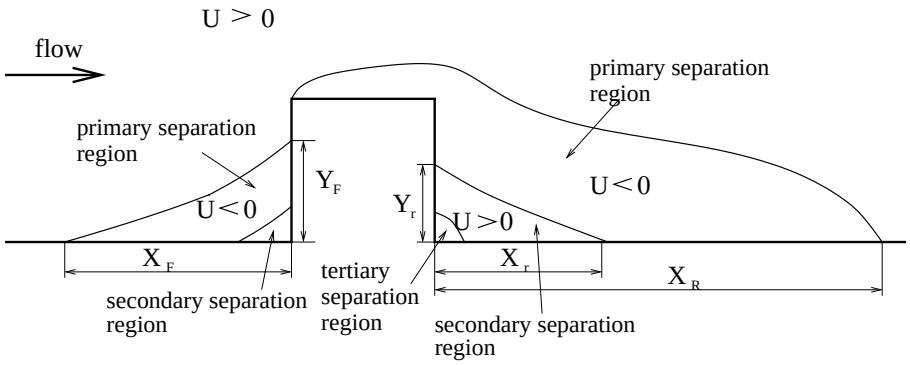

Figure 18: Schematic representation of separation and reattachment regions.

	X_R	X_r	Y_r	X_F	Y_F
DNS [41]	6.42	1.21	0.35	1.51	0.28
LES [41]	6.80	1.13	0.36	1.51	0.37
Scheme 1	5.97	0.87	0.42	0.9	0.40
Scheme 2	6.40	1.29	0.35	1.31	0.39

Table 1: Separation and reattachment lengths computed in different types of simulations.

nates, are plotted in figures 22-23. The quantities are averaged in the homogeneous direction and in time over 40 characteristic time units. The present results are compared with direct numerical simulations (DNS) [21], [41], LES [41] and experimental data [13].

It can be noticed that in the separation region above and behind the obstacle, scheme 2 yields significantly better results than scheme 1. Above the cylinder, the streamwise and normal velocity profiles for scheme 1 are more disturbed, possibly due to the noise in the vorticity production on the upstream corner.

For $Re = 5000$, the standard finite difference method leads to numerical instability and entirely erroneous results. Using the vorticity preserving method, instead, results consistent with those in the $Re = 3000$ case are obtained and displayed in figures 24-25.

9 Conclusions and open issues

A vorticity preserving discretization of the three-dimensional, incompressible Navier-Stokes equations has been presented, which includes an appropriate treatment for viscous terms and rigid wall boundary conditions. Numerical re-

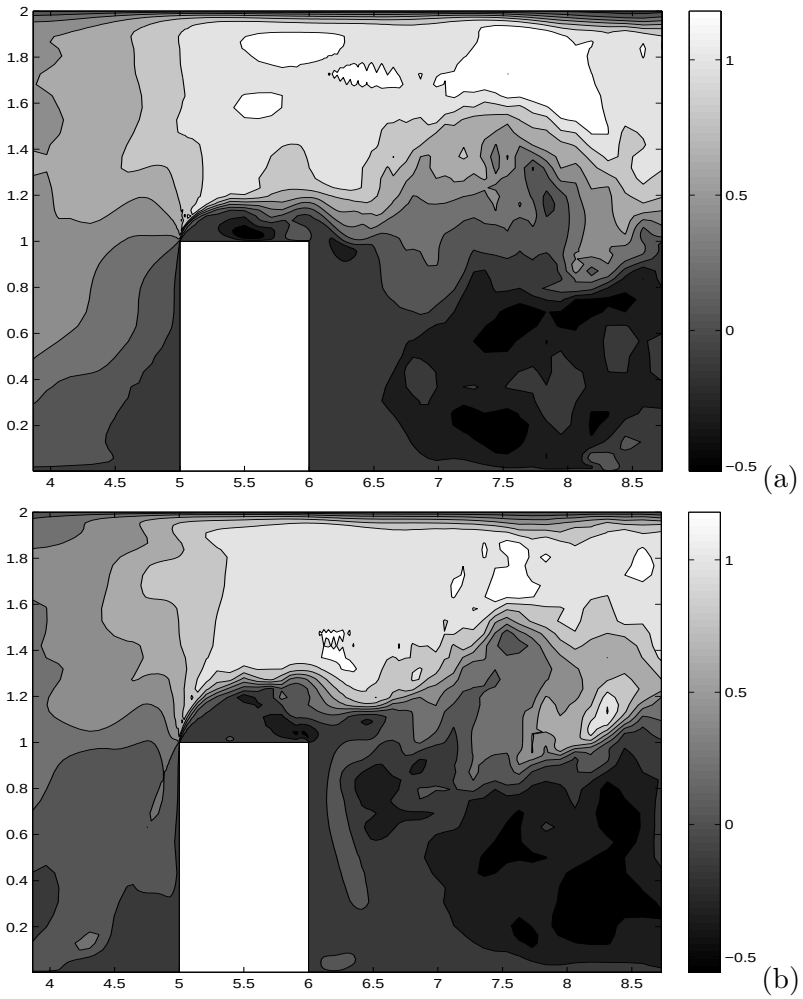

Figure 19: Instantaneous streamwise velocity field computed with (a) scheme 1 and (b) scheme 2.

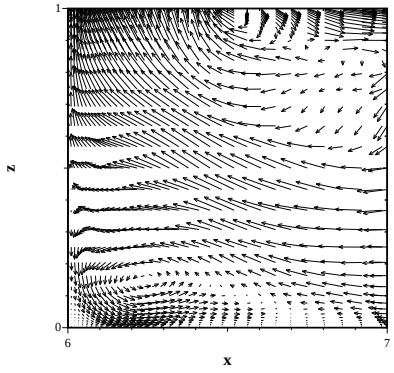

(a)

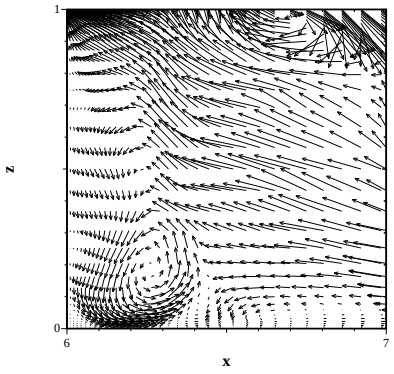

(b)

Figure 20: Instantaneous velocity field in the downstream corner computed with (a) scheme 1 and (b) scheme 2.

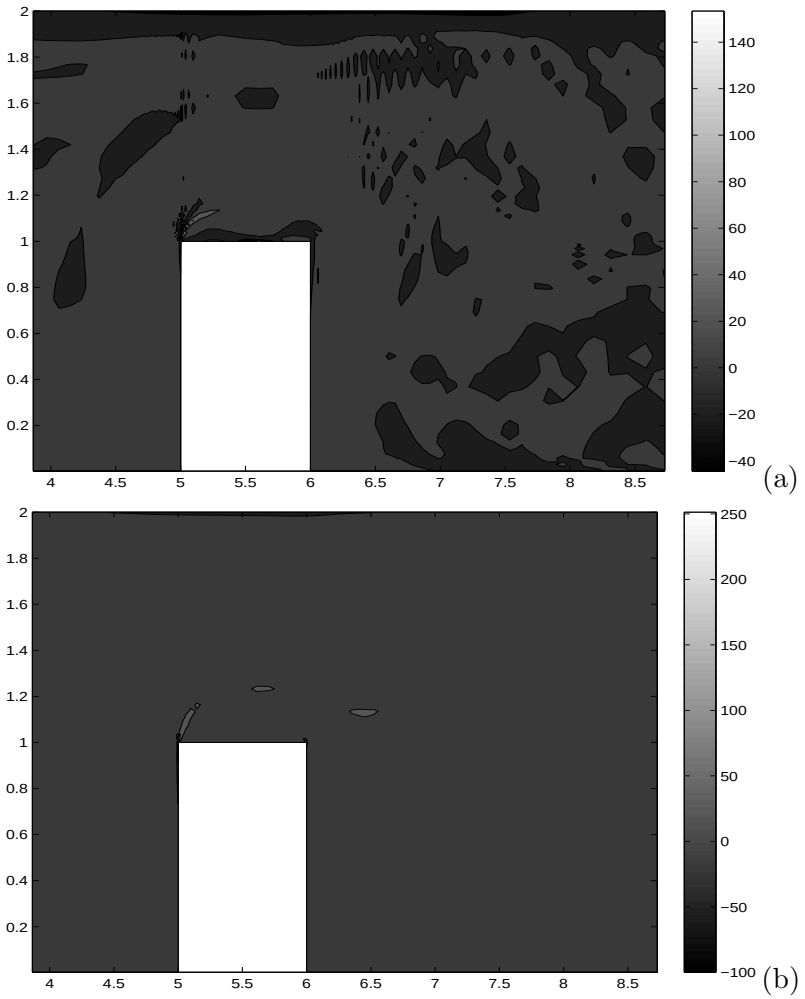

Figure 21: Instantaneous transversal vorticity field on the upstream corner computed with (a) scheme 1 and (b) scheme 2.

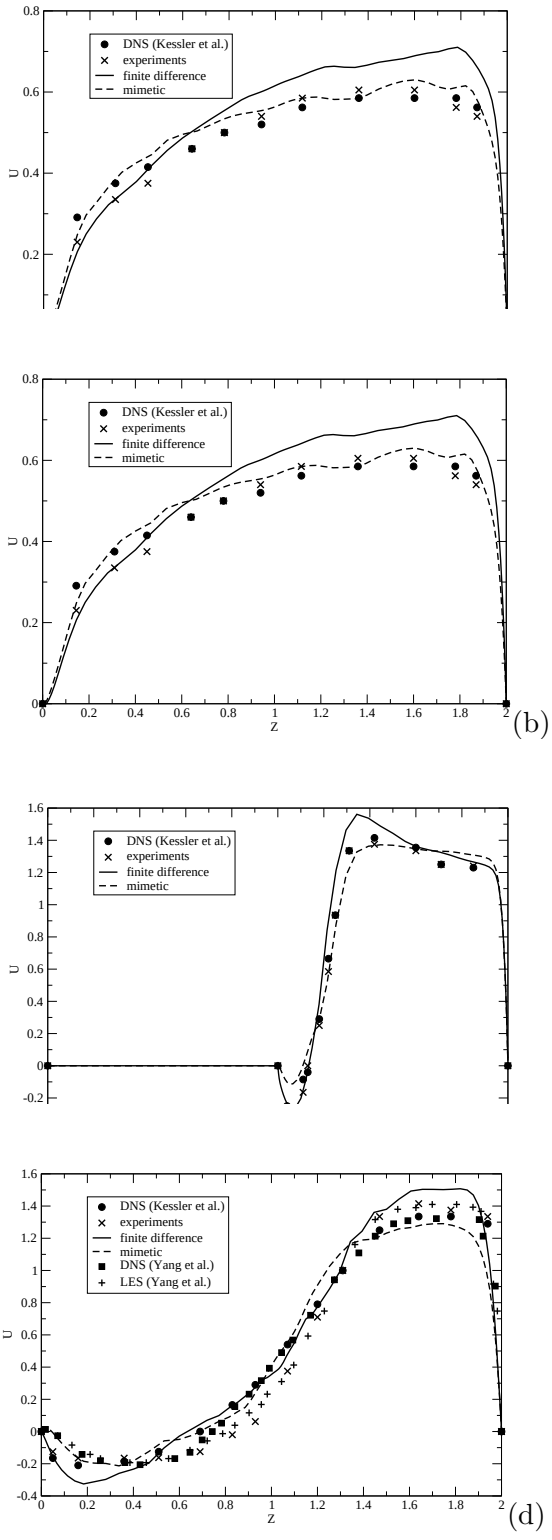

Figure 22: Averaged streamwise velocity profile at locations (a) $x = 3.8$, (b) $x = 5.08$,(c) $x = 5.5$ and (d) $x = 7$. •: DNS [21]; □: DNS [41]; +: LES [41]; ×: experimental data [13]; : scheme 1; −−: scheme2.

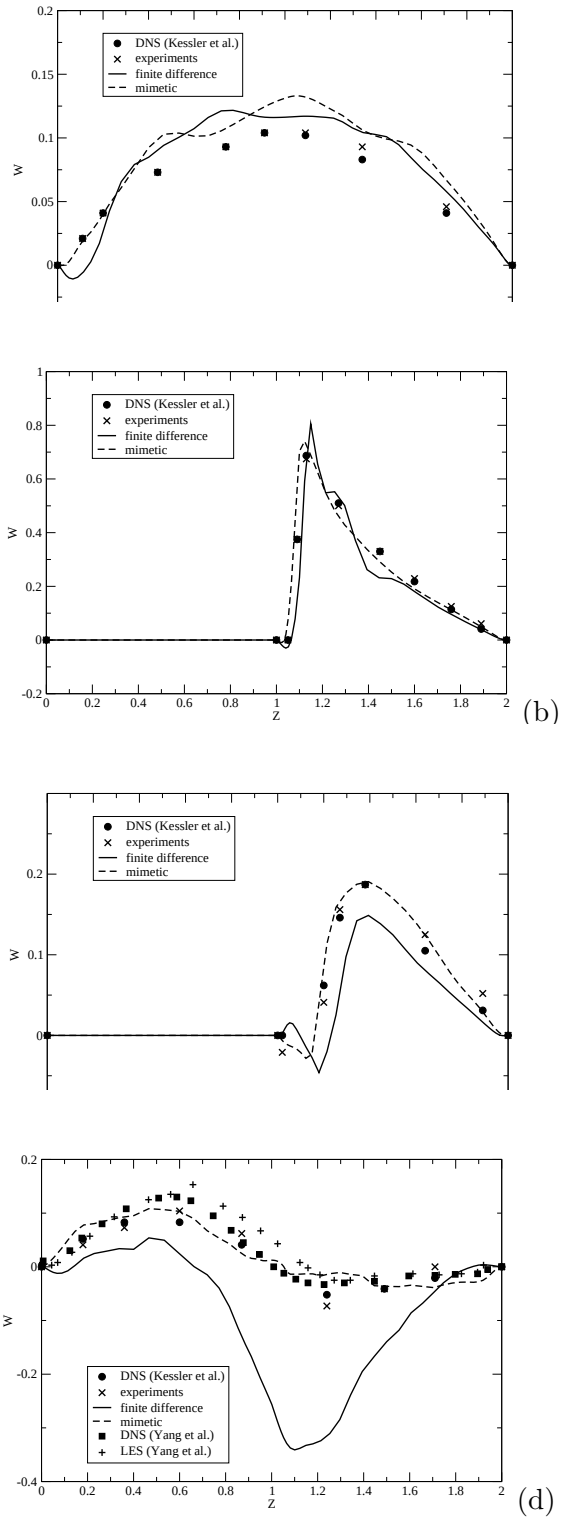

Figure 23: Averaged vertical velocity profile at locations (a) $x = 3.8$, (b) $x = 5.08$,(c) $x = 5.5$ and (d) $x = 7$. •: DNS [21]; □: DNS [41]; +: LES [41]; ×: experimental data [13]; : scheme 1; −−: scheme2.

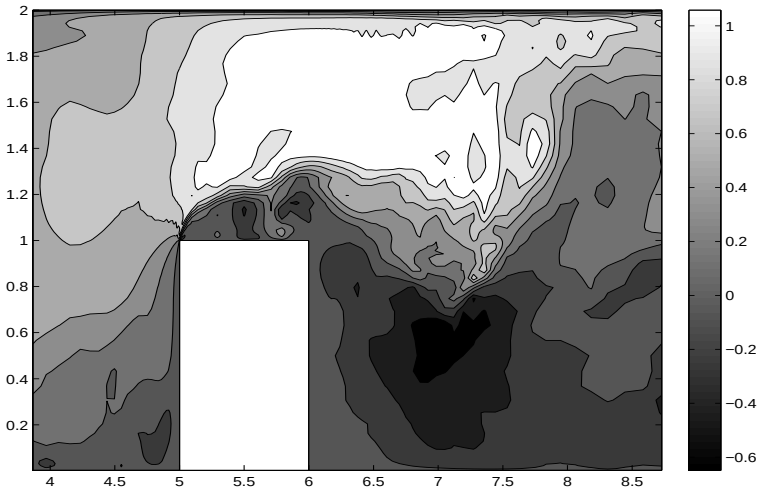

Figure 24: Instantaneous streamwise velocity field around the cube at $Re = 5000$, vorticity preserving method.

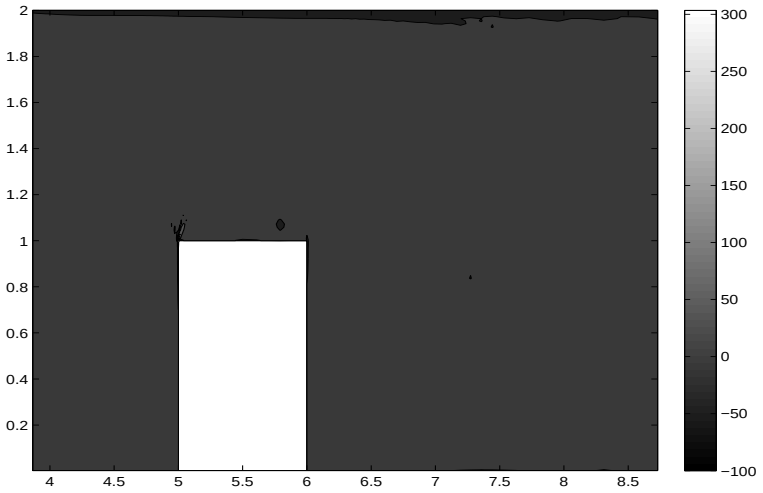

Figure 25: Instantaneous transversal vorticity component around the cube at $Re = 5000$, vorticity preserving method.

sults obtained in a number of test cases show that the method has considerable advantages with respect to another finite difference scheme of the same order of accuracy, especially in regimes where highly localized vorticity production is taking place close to boundaries and the resolution is relatively coarse. In particular, remarkable accuracy was achieved in a LES simulation of a high Reynolds number benchmark, for which the results of the proposed method were compared successfully to those of DNS simulations and to experimental data.

These results seem to support the heuristic considerations in [29] and motivate further research and analysis. In particular, we would like to carry out a more systematic assessment of the relative merits of the present approach with respect to energy preserving methods such as those proposed in [18], [33] and with respect to other finite volume and finite element discretizations. Extension to unstructured three dimensional meshes along the lines of the two dimensional methods proposed in [10], [33] are also feasible and will be investigated.

Acknowledgements

We would like to thank the anonymous reviewers of a previous version of this paper for many useful comments and for suggesting some of the numerical tests carried out here.

References

[1] A. Abbà and L. Bonaventura. A mimetic finite difference discretization for the incompressible Navier-Stokes equations. Technical Report 83, MOX - Politecnico di Milano, 2006.

[2] A. Abbà and L. Bonaventura. A mimetic finite difference discretization for the incompressible Navier-Stokes equations. *International Journal of Numerical Methods in Fluids*, 56:1101–1106, 2008.

[3] A. Abbà, C. Cercignani, and L. Valdettaro. Analysis of subgrid scale models. *Computers and Mathematics with Applications*, 46(4):521–536, 2003.

[4] A.S. Almgren, J.B. Bell, P. Colella, L. Howell, and M.L. Welcome. A conservative adaptive projection method for the variable density incompressible Navier-Stokes equations. *Journal of Computational Physics*, 142:1–46, 1998.

[5] A. Arakawa and V. Lamb. A potential enstrophy and energy conserving scheme for the shallow water equations. *Monthly Weather Review*, 109:18–136, 1981.

[6] A. Arakawa and M. Suarez. Vertical differencing of the primitive equations in sigma coordinates. *Monthly Weather Review*, 111:34–45, 1983.

[7] P. Ashwin and O. Podvigina. Hopf bifurcation with cubic symmetry and instability of ABC flow. *Proceedings of the Royal Society of London A*, 459:1801–1827, 2003.

[8] F. Bertagnolio and O. Daube. Three-dimensional incompressible Navier - Stokes equations on non-orthogonal staggered grids using the velocity-vorticity formulation. *International Journal of Numerical Methods in Fluids*, 28:917–943, 1998.

[9] L. Bonaventura, L. Kornblueh, T. Heinze, and P. Ripodas. A semi-implicit method conserving mass and potential vorticity for the shallow water equations on the sphere. *International Journal of Numerical Methods in Fluids*, 47:863–869, 2005.

[10] L. Bonaventura and T. Ringler. Analysis of discrete shallow water models on geodesic Delaunay grids with C-type staggering. *Monthly Weather Review*, 133:2351–2373, 2005.

[11] A. Bracco, J.C. McWilliams, G. Murante, A. Provenzale, and J.B. Weiss. Revisiting freely decaying two-dimensional turbulence at millennial resolution. *Physics of Fluids*, 12:2931–2941, 2000.

[12] A. Chorin and J. E. Marsden. *A Mathematical Introduction to Fluid Mechanics.* Springer Verlag, 1993.

[13] G. Dimaczek, R. Kessler, R. Martinuzzi, and C. Tropea. The flow over two-dimensional, surface mounted obstacles at high Reynolds number. In *Proceedings of the 7th Symposium on Turbulent Shear Flows, Stanford*. Stanford University, 1989.

[14] D. Galloway and U. Frisch. A note on the stability of a family of space-periodic Beltrami flows. *Journal of Fluid Mechanics*, 180:557–564, 1987.

[15] M. Germano, U. Piomelli, P. Moin, and H. Cabot. A dynamic subgrid-scale eddy viscosity model. *Physics of Fluids A*, 3:1760–1765, 1991.

[16] P.M. Gresho and S.T. Chan. On the theory of semi-implicit projection methods, part 2: implementation. *International Journal of Numerical Methods in Fluids*, 11:621–659, 1990.

[17] F.H. Harlow and J.E. Welsh. Numerical calculation of time-dependent viscous incompressible flow of fluid with free surface. *Physics of Fluids*, 8:2182–2189, 1965.

[18] J.E. Hicken, F.E. Ham, J. Militzer, and M. Koksal. A shift transformation for fully conservative methods: turbulence simulation on complex, unstructured grids. *Journal of Computational Physics*, 208:704–734, 2005.

[19] J. Hyman and M. Shashkov. The orthogonal decomposition theorems for mimetic finite difference methods. *SIAM Journal of Numerical Analysis*, 36:788–818, 1999.

[20] Z.I. Janjic. Nonlinear advection schemes and energy cascade on semi-staggered grids. *Monthly Weather Review*, 111:1234–1245, 1984.

[21] R. Kessler and K.S. Yang. Direct numerical simulation of turbulent obstacle flow. In *Direct and Large-Eddy Simulation II*, 1997.

[22] J. Kim and P. Moin. Application of a fractional-step method to incompressible Navier-Stokes equations. *Journal of Computational Physics*, 59:308–323, 1985.

[23] H. Kreplin and M. Eckelmann. Behaviour of the three fluctuating velocity components in the wall region of a turbulent channel flow. *Physics of Fluids*, 22:1233–1239, 1979.

[24] H. Le and P. Moin. An improvement of fractional-step methods for the incompressible Navier-Stokes equations. *Journal of Computational Physics*, 92:369–379, 1991.

[25] D.K. Lilly. A proposed modification of the Germano subgrid-scale closure method. *Physics of Fluids A*, 4:633–635, 1992.

[26] S.J. Lin and R.B. Rood. An explicit flux-form semi-Lagrangian shallow water model on the sphere. *Quarterly Journal of the Royal Meteorological Society*, 123:2477–2498, 1997.

[27] F. Mesinger. Horizontal advection schemes on a staggered grid: an enstrophy and energy conserving model. *Monthly Weather Review*, 109:467–478, 1981.

[28] Y. Morinishi, T.S.Lund, O.V. Vasilyev, and P. Moin. Fully conservative higher order finite difference schemes for incompressible flow. *Journal of Computational Physics*, 143:90–124, 1998.

[29] K.W. Morton and P.L. Roe. Vorticity preserving Lax-Wendroff type schemes for the system wave equation. *SIAM Journal of Scientific Computing*, 23:170–192, 2001.

[30] R. D. Moser, J. Kim, and N. N. Mansour. Direct numerical simulation of turbulent channel flow up to $re_\tau = 590$.. *Physic of Fluids*, 11:943, 1999.

[31] R.A. Nicolaides. Direct discretization of planar div-curl problems. *SIAM Journal of Numerical Analysis*, 29:32–56, 1992.

[32] R.A. Nicolaides and X. Wu. Analysis and convergence of the MAC scheme II: Navier-Stokes equations. *Mathematics of Computation*, 65:29–44, 1996.

[33] B. Perot. Conservation properties of unstructured staggered mesh schemes. *Journal of Computational Physics*, 159:58–89, 2000.

[34] A. Quarteroni and A. Valli. *Numerical Approximation of Partial Differential Equations*. Springer, Berlin-Heidelberg, 1994.

[35] T.D. Ringler and D.A. Randall. A potential enstrophy and energy conserving numerical scheme for solution of the shallow-water equations a geodesic grid. *Monthly Weather Review*, 130:1397–1410, July 2002.

[36] R. Sadourny. The dynamics of finite difference models of the shallow water equations. *Journal of the Atmospheric Sciences*, 32:680–689, 1975.

[37] G. J. Tripoli. A nonhydrostatic mesoscale model designed to simulate scale interaction. *Monthly Weather Review*, 120:1343–1359, 1992.

[38] E W. and J.G. Liu. Vorticity boundary condition and related issues for finite difference schemes. *Journal of Computational Physics*, 124:368–382, 1996.

[39] I. Wenneker, A. Segal, and P. Wesseling. A mach uniform unstructured staggered method. *International Journal of Numerical Methods in Fluids*, 40:1209–1235, 2002.

[40] I. Wenneker, A. Segal, and P. Wesseling. Conservation properties of a new unstructured staggered scheme. *Computers and Fluids*, 124:139–147, 2003.

[41] K. S. Yang and J.H. Ferziger. Large-Eddy Simulation of turbulent obstacle flow using a dynamic subgrid scale model. *AIAA Journal*, 31:1406–1413, 1993.

[42] R.J. Adrian Z.-C. Liu, C.C. Landreth and T.J. Hanratty. High resolution measurements of turbulent structure in a channel with particle image velocimetry. *Experiments in Fluids*, 10:301–312, 1991.

MOX Technical Reports, last issues

Dipartimento di Matematica "F. Brioschi",
Politecnico di Milano, Via Bonardi 9 - 20133 Milano (Italy)

34/2010 Antonella Abba', Luca Bonaventura:
A mimetic finite difference method for Large Eddy Simulation of incompressible flow

33/2010 Giovanni Migliorati, Alfio Quarteroni:
Multilevel Schwarz Methods for Elliptic Partial Differential Equations

32/2010 A. Cristiano I. Malossi, Pablo J. Blanco,
Simone Deparis, Alfio Quarteroni:
Algorithms for the partitioned solution of weakly coupled fluid models for cardiovascular flows

31/2010 Andrea Manzoni, Alfio Quarteroni, Gianluigi Rozza:
Shape optimization for viscous flows by reduced basis methods and free-form deformation

30/2010 Pablo J. Blanco, Marco Discacciati,
Alfio Quarteroni:
Modeling dimensionally-heterogeneous problems: analysis, approximation and applications

29/2010 Matteo Lesinigo, Carlo D'Angelo, Alfio Quarteroni:
A multiscale Darcy-Brinkman model for fluid flow in fractured porous media

28/2010 Paolo Crosetto, Philippe Reymond, Simone Deparis,
Dimitrios Kontaxakis, Nikolaos Stergiopulos,
Alfio Quarteroni:
Fluid Structure Interaction Simulations of Physiological Blood Flow in the Aorta

27/2010 Matteo Bruggi, Marco Verani:
An adaptive algorithm for topology optimization with goal-oriented error control

26/2010 Francesca Ieva, Anna Maria Paganoni:
Designing and mining a multicenter observational clinical registry concerning patients with Acute Coronary Syndromes

25/2010 G. Pena, C. Prud'homme, Alfio Quarteroni:
High Order Methods for the Approximation of the Incompressible Navier-Stokes Equations in a Moving Domain